6. J. S. Kargel, S. Pozio, *Icarus* **119**, 385 (1996).
7. J. Lewis, *Icarus* **15**, 174 (1971).
8. S. J. Peale, *Annu. Rev. Astron. Astrophys.* **37**, 533 (1999).
9. J. Wisdom, *Astron. J.* **128**, 484 (2004).
10. M. K. Dougherty *et al.*, *Science* **311**, 1406 (2006).
11. R. H. Brown *et al.*, *Science* **311**, 1425 (2006).
12. C. C. Porco *et al.*, *Space Sci. Rev.* **115**, 363 (2004).
13. J. R. Spencer *et al.*, *Science* **311**, 1401 (2006).
14. ISS and CIRS are acknowledged in the codiscovery of the correlation between the hottest temperatures measured in the SPT and the tiger stripe fractures.
15. F. Spahn *et al.*, *Science* **311**, 1416 (2006).
16. J. H. Waite Jr. *et al.*, *Science* **311**, 1419 (2006).
17. C. J. Hansen *et al.*, *Science* **311**, 1422 (2006).
18. G. H. Jones *et al.*, *Science* **311**, 1412 (2006).
19. G. Hansen, personal communication.
20. C. C. Porco *et al.*, *Science* **307**, 1237 (2005).
21. G. Neukum *et al.*, *Lunar Planet. Sci. Conf. 36*, abstract 2034 [CD-ROM] (2005).
22. R. Wagner *et al.*, *Bull. Am. Astron. Soc.* **37**, 701 (2005).
23. G. Neukum, thesis, Ludwig-Maximilians-Universität München (1983).
24. G. P. Horedt, G. Neukum, *J. Geophys. Res.* **89**, 10405 (1984).
25. G. Neukum, *Adv. Space Res.* **5**, 107 (1985).
26. R. Ionasescu, *Jet Propulsion Laboratory Interoffice Memorandum IOM 343J-05-017* (2 May 2005).
27. R. Jacobson and the Cassini Project Navigation team, personal communication.
28. S. F. Dermott, *Icarus* **37**, 575 (1979).
29. S. F. Dermott, P. C. Thomas, *Icarus* **109**, 241 (1994).
30. Brightness values were converted into particle densities with the use of an assumed analytical particle size distribution (*42*): $n(r) = $ constant $r^{(1-3b)/b} \exp(-r/ab)$, where a is the effective radius (1.0 μm, appropriate for particles in the E ring) and $b = 0.25$. The quantity b is large enough to ensure a fair fraction of the particles are large enough (i.e., >2 μm) for CDA to detect. Horizontal (line-of-sight) column densities, N_{los}, were computed from the peak I/F by the relation $N_{los} = 4(I/F)/[A_{sca} \times P(\varphi)]$, where A_{sca} is the scattering cross section appropriate for the chosen particle size distribution, and $P(\varphi)$ is the phase function computed for Mie scatterers at phase angle φ. The scattering cross section used for the assumed particle size distribution and an effective observation wavelength of 569 nm was 3.12 square μm; $P(\varphi = 161.4) = 6.688$.
31. A. Juhasz, M. Horanyi, *J. Geophys. Res.* **107**, A6 1066 (2002).
32. M. Hedman, personal communication.
33. J. Eluszkiewicz, J.-L. Moncet, *Icarus* **166**, 375 (2003).
34. S. W. Kieffer, in *The Satellites of Jupiter*, D. Morrison, Ed. (Univ. of Arizona Press, Tucson, AZ, 1982), pp. 647–723.
35. E. J. Gaidos, F. Nimmo, *Nature* **405**, 637 (2000).
36. D. L. Goldsby, D. L. Kohlstedt, *J. Geophys. Res.* **106**, 11017 (2001).
37. C. F. Yoder, *Nature* **279**, 767 (1979).
38. G. Schubert, T. Spohn, R. T. Reynolds, in *Satellites*, J. A. Burns, M. S. Matthews, Eds. (Univ. of Arizona Press, Tucson, AZ, 1986), pp. 224–292.
39. M. N. Ross, G. Schubert, *Icarus* **78**, 90 (1989).
40. P. Helfenstein, E. M. Parmentier, *Icarus* **53**, 415 (1983).
41. H. J. Melosh, *Icarus* **31**, 221 (1977).
42. J. E. Hansen, *J. Atmos. Sci.* **28**, 1400 (1971).
43. G. Neukum, B. A. Ivanov, W. K. Hartmann, *Space Sci. Rev.* **96**, 55 (2001).
44. K. Zahnle, P. Schenk, H. Levison, L. Dones, *Icarus* **163**, 263 (2004).
45. We acknowledge the financial support of NASA/JPL, the UK Particle Physics and Astronomy Research Council, the Deutsches Zentrum fur Luft- und Raumfahrt (German Aerospace Center), and Université Paris VII Denis Diderot, Commissariat à l'Energie Atomique, Astrophysique Interactions Multieschelle, France.

RESEARCH ARTICLE

Cassini Encounters Enceladus: Background and the Discovery of a South Polar Hot Spot

J. R. Spencer,[1]* J. C. Pearl,[2] M. Segura,[2] F. M. Flasar,[2] A. Mamoutkine,[2] P. Romani,[2] B. J. Buratti,[3] A. R. Hendrix,[3] L. J. Spilker,[3] R. M. C. Lopes[3]

The Cassini spacecraft completed three close flybys of Saturn's enigmatic moon Enceladus between February and July 2005. On the third and closest flyby, on 14 July 2005, multiple Cassini instruments detected evidence for ongoing endogenic activity in a region centered on Enceladus' south pole. The polar region is the source of a plume of gas and dust, which probably emanates from prominent warm troughs seen on the surface. Cassini's Composite Infrared Spectrometer (CIRS) detected 3 to 7 gigawatts of thermal emission from the south polar troughs at temperatures up to 145 kelvin or higher, making Enceladus only the third known solid planetary body—after Earth and Io—that is sufficiently geologically active for its internal heat to be detected by remote sensing. If the plume is generated by the sublimation of water ice and if the sublimation source is visible to CIRS, then sublimation temperatures of at least 180 kelvin are required.

Cassini-Huygens is a major international planetary mission that entered orbit around Saturn on 1 July 2004 for a nominal 4-year investigation of the planet, its satellites, rings, and magnetosphere. In 2005, Cassini made three flybys of the enigmatic satellite Enceladus, long suspected to be recently geologically active and the source of Saturn's tenuous, extended E ring. Results from multiple Cassini instruments on the third flyby on 14 July 2005 offer convincing proof that this small icy satellite is currently active, as described in this series of companion papers.

Enceladus. Discovered by William Herschel in 1789, Enceladus orbits close to Saturn at a radius of 3.94 Saturn radii and thus is difficult to observe from Earth because of the scattered light of the planet and its rings. Enceladus' orbital period is 1.37 days. Telescopic infrared spectra indicate a surface composed of almost pure water ice (*1*), although a tentative detection of ammonia ice has been reported recently (*2*). The Voyager encounters with the satellite in 1981 established its radius (252.1 km) (*3*) and that its visual geometric albedo is startlingly high, consistent with fresh snow or ice, and higher than for any other known solar system body (*4, 5*). Voyager 2 also discovered that Enceladus was unique among Saturn's medium-sized icy satellites, be-

cause its surface includes sizable crater-free areas that have been resurfaced by endogenic forces (*4*) and were estimated to be <200 million years old (*6*). Other parts of the satellite are heavily cratered and perhaps nearly as old as the solar system, but the craters show considerable signs of internal modification. All regions of the satellite, regardless of age, exhibit uniformly high albedos, implying that the entire satellite is coated with a ubiquitous fresh material (*7*). Particle-orbit models have shown that Enceladus is probably the major source of the tenuous E ring (*8*), which is most dense at the satellite's orbit. The mechanism for the injection of material from the satellite into the E ring has been debated; volcanism (*9*), geysers (*10*), large impacts (*11*), and collisions between Enceladus and E-ring particles themselves (*12*) have all been proposed. Regardless of the means of transport, the micrometer-sized particles that make up the ring must be constantly replenished, because sputtering (*10, 13*) would destroy them on time scales much shorter than the age of the solar system.

The heat source for the extensive resurfacing on an object as small as Enceladus has always been difficult to explain, especially when compared to other saturnian satellites that show much less evidence of activity (*14–16*). The orbital eccentricity of Enceladus (0.0047, comparable to that of Io) is perhaps sufficient for substantial

[1]Department of Space Studies, Southwest Research Institute, 1050 Walnut Street, Suite 400, Boulder, CO 80302, USA. [2]NASA Goddard Spaceflight Center, Code 693, Greenbelt, MD 20771, USA. [3]Jet Propulsion Laboratory, California Institute of Technology, 4800 Oak Grove Drive, Pasadena, CA 91109, USA.

*To whom correspondence should be addressed. E-mail: spencer@boulder.swri.edu

tidal heating given the right internal structure (*16*), but the absence of internal activity on nearby Mimas, which has an orbital eccentricity of 0.0202, makes this source problematic, too. The contrast with Mimas might be explained if Mimas is in a cold, elastic, nondissipative state, whereas Enceladus is in a self-maintaining warm, plastic, dissipative state (*17*). Resonantly excited rotational librations have recently been suggested as a possible alternative tidal heating mechanism (*18, 19*).

Cassini flybys. Cassini has observed Enceladus with multiple instruments including the Ultraviolet Imaging Spectrograph (UVIS), the visible-wavelength Imaging Science Subsystem (ISS), the Visual and Infrared Mapping Spectrometer (VIMS), the Composite Infrared Spectrometer (CIRS), the magnetometer (MAG), the Cosmic Dust Analyzer (CDA), the Cassini Plasma Spectrometer (CAPS), the Radio and Plasma Wave Science (RPWS) instrument, and the Ion and Neutral Mass Spectrometer (INMS). The first close Cassini flyby of Enceladus, on orbit 3 on 17 February 2005 at an altitude of 1258.6 km (Table 1), focused on the equatorial region centered near longitude 310°W. ISS revealed a world scarred by extensive tectonic activity (*19*), and VIMS spectra indicated that the surface composition was completely dominated by water ice (*20*). MAG data showed a draping of Saturn's magnetic field lines around the moon, which suggested the presence of an atmosphere (*21*). However, UVIS observations of a stellar occultation showed no sign of an atmosphere at low latitudes (*22*). During the second flyby, on orbit 4 at an altitude of 497.0 km on 9 March 2005, Cassini concentrated on the equatorial region of the hemisphere centered near 190°W. ISS images revealed complex networks of ridges and troughs coexisting with ancient cratered plains. MAG measured a signature in addition to the one seen in February, possibly indicating an induced or intrinsic magnetic field. Based on the MAG results, the Cassini Project decided to reduce the altitude of the 14 July 2005 encounter, on orbit 11, from 1000 km down to ~170 km.

On the 14 July flyby, the spacecraft approached the illuminated anti-Saturn hemisphere, which is centered on longitude 180°W, from the south. On approach, the remote sensing instruments (ISS, VIMS, UVIS, and CIRS) observed Enceladus beginning 8 hours before the closest approach, starting from a distance of 288,000 km. At 21 min before the closest approach, the spacecraft began the turn to point to the star γ-Orionis (Bellatrix), and at 4 min before the closest approach, Bellatrix was occulted by Enceladus; measurements of the occultation were performed by UVIS (*22*). As Enceladus passed in front of the star, the moon crossed through the boresights of the remote sensing instruments, providing a brief opportunity for remote sensing at very high spatial resolution. The subspacecraft point at the closest approach

was at 24°S, 326°W. After the occultation, at 3 min after the closest approach, the spacecraft began to turn back to Enceladus and resumed remote sensing of the nighttime surface at 31 min after the closest approach, continuing to 114 min. Throughout the inbound and outbound portions of the flyby and during the closest approach, the fields and particles instruments obtained valuable information on the plasma and particulate environment around Enceladus. In particular, INMS (*23*), CAPS,

RPWS (*24*), and CDA (*25*) obtained in situ measurements of the near–south polar environment.

Composite Infrared Spectrometer results. The CIRS instrument (*26*) used the three Enceladus encounters to investigate the satellite's thermal radiation, which provides clues to its surface properties and a means to detect possible endogenic activity. The only previous observations of Enceladus' thermal radiation were by Voyager 2 in 1981 (*27*), which derived a disk-

Table 1. Cassini Enceladus encounter geometries. Times are in universal time at the spacecraft.

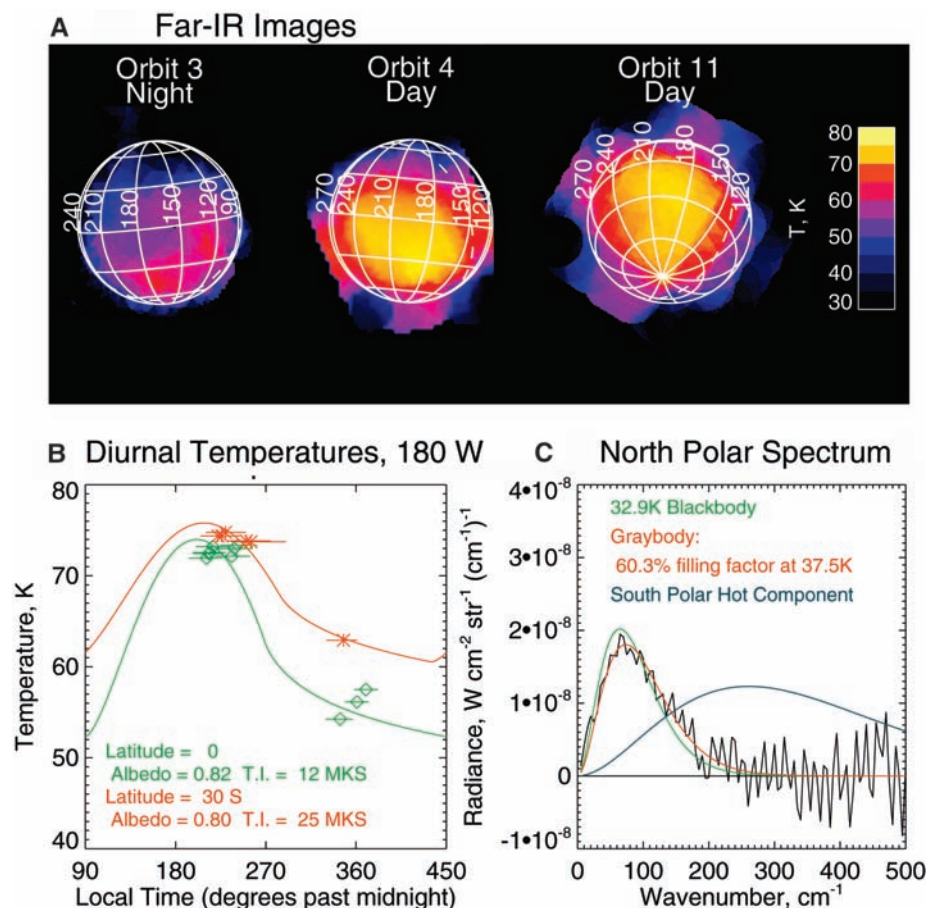| Cassini orbit	Date	Time	Altitude at closest approach (km)	Approach geometry 2 hours before encounter	
				Subspacecraft latitude, longitude	Phase angle
3	17 February 2005	03:30	1258.6	309°W, 0°N	25
4	9 March 2005	09:08	497.0	191°W, 1°S	47
11	14 July 2005	19:55	168.2	186°W, 47°S	47

Fig. 1. Far-IR observations of Enceladus. (**A**) Far-IR brightness temperature images of the nighttime and daytime thermal emission from the anti-Saturn hemisphere of Enceladus (centered at longitude 180°W) from the three Cassini encounters. The apparent signal beyond the limb of Enceladus is an artifact of the low spatial resolution and the plotting technique. (**B**) Thermal model fits to the far-IR day and night brightness temperatures at longitude 180°W and two different latitudes, as measured on orbits 3 and 4, showing the large spatial variations in thermal inertia [TI, in m kg s (MKS units)]. Horizontal bars show the local time range of each observation. (**C**) Far-IR spectrum of the north pole, with best fit blackbody and graybody spectra, showing the lack of the high-temperature component seen at the south pole. The fine structure in this and all spectra shown is due to noise.

integrated 250-cm^{-1} brightness temperature (*28*) of 67 K at 37° phase angle with an inferred subsolar temperature of 75 ± 3 K, but provided little other information. CIRS consists of two Fourier transform spectrometers, which together measure thermal emission from 10 to 1400 cm^{-1} (wavelengths 1 mm to 7 μm) at a selectable spectral resolution between 0.5 and 15.5 cm^{-1}. The far-infrared interferometer (10 to 600 cm^{-1}) has a 4-mrad field of view on the sky. The mid-infrared (IR) interferometer consists of two 1 × 10 arrays of 0.3-mrad pixels, which together span 600 to 1400 cm^{-1}.

Cassini's first two flybys of Enceladus, in February and March 2005, provided good views of the low-latitude regions on both sides of the satellite. Daytime thermal emission from the anti-Saturn side of the moon was mapped by the far-IR detector in March 2005, and the same region was seen at night in February 2005 (Fig. 1A). Most

spectra are well described by blackbody curves in the 50 to 600 cm^{-1} range, and we estimate surface temperature by least squares fitting of blackbody curves to the spectra. Comparison of daytime and nighttime temperatures for the same regions allows for the determination of bolometric albedo and thermal inertia (*29*) as a function of location on this hemisphere. Nighttime temperatures showed spatial variability, probably resulting from thermal inertia variations. Day and night temperatures near longitude 180°W can be matched by models with thermal inertias in the range 12 to 25 J m^{-2} s$^{-1/2}$ K^{-1}, averaged over the uppermost ~1 cm of the surface layer, whereas bolometric albedo on this hemisphere is more constant, varying between 0.80 and 0.82 (Fig. 1B). These bolometric albedos are consistent with the estimate from Voyager photometry of 0.90 ± 0.10 (*30*), and subsolar temperatures near 76 K are also consistent with Voyager es-

timates (*27*). The thermal inertia is 100 times smaller than that of solid water ice (*31*), implying a highly unconsolidated surface.

The third flyby, on orbit 11 on 14 July 2005, provided the first good view of the south polar regions of Enceladus. Maps of the daytime thermal emission were obtained with both the mid-IR and far-IR detectors on approach. The low spatial resolution of the far-IR detector prevented good observations of the south polar region at long wavelengths (Fig. 1A), but the mid-IR detector was able to map the entire disk at a spatial resolution of 25 km over the 600- to 800-cm^{-1} (12.5 to 16 μm) spectral range, with useful signal at higher wave numbers in the warmest regions (Fig. 2, A and B). The equatorial regions showed 650-cm^{-1} brightness temperatures in the high 70s K, consistent with models of passive solar heating based on the range of thermal inertias and albedos determined from the earlier flybys (Fig. 1). However, most of the polar region south of latitude 65°S showed higher brightness temperatures, reaching 85 K near the south pole. This temperature is surprisingly warm; the temperature at the south pole, which is in equilibrium with current insolation (i.e., assuming zero thermal inertia), is only 68 K for an albedo of 0.81 because of the highly oblique illumination there (solar elevation at the pole was only 23°). An implausibly low south polar albedo of 0.55, 67% of the equatorial albedo, would be necessary to increase the equilibrium temperature to 85 K. The elevated temperatures are not due to seasonal effects; we modeled long-term seasonal variations in the south polar temperature due to changes in the subsolar latitude and heliocentric distance of Enceladus for a range of thermal inertias, and we found that at the current season (midway between the southern summer solstice and the fall equinox), the south polar temperature is lower still for nonzero thermal inertia. The region of elevated south polar temperatures corresponds closely to a geologically youthful region occupied by four prominent troughs (dubbed "tiger stripes") seen by the Cassini cameras (Fig. 2B) (*19*).

The spectrum of the south polar thermal emission yields evidence for even higher temperatures, making an origin from solar heating even less likely. We found that the south polar spectrum was not well fit by a single-temperature blackbody filling the field of view. After subtracting the expected background thermal emission from a solar-heated surface, assuming a model with an albedo of 0.81 and thermal inertia of 20 J m^{-2} s$^{-1/2}$ K^{-1}, the average spectrum of the 37,000-km^2 region south of 65°S could be fitted perfectly, within the uncertainties, by a graybody (i.e., a blackbody multiplied by a wavelength-independent filling factor). The best fit graybody has a temperature of 133 ± 12 K occupying 345$^{+320}_{-160}$ km^2, where the superscript and subscript are the errors (Fig. 2C). We determined uncertainties in the fit parameters by a Monte Carlo technique. We first
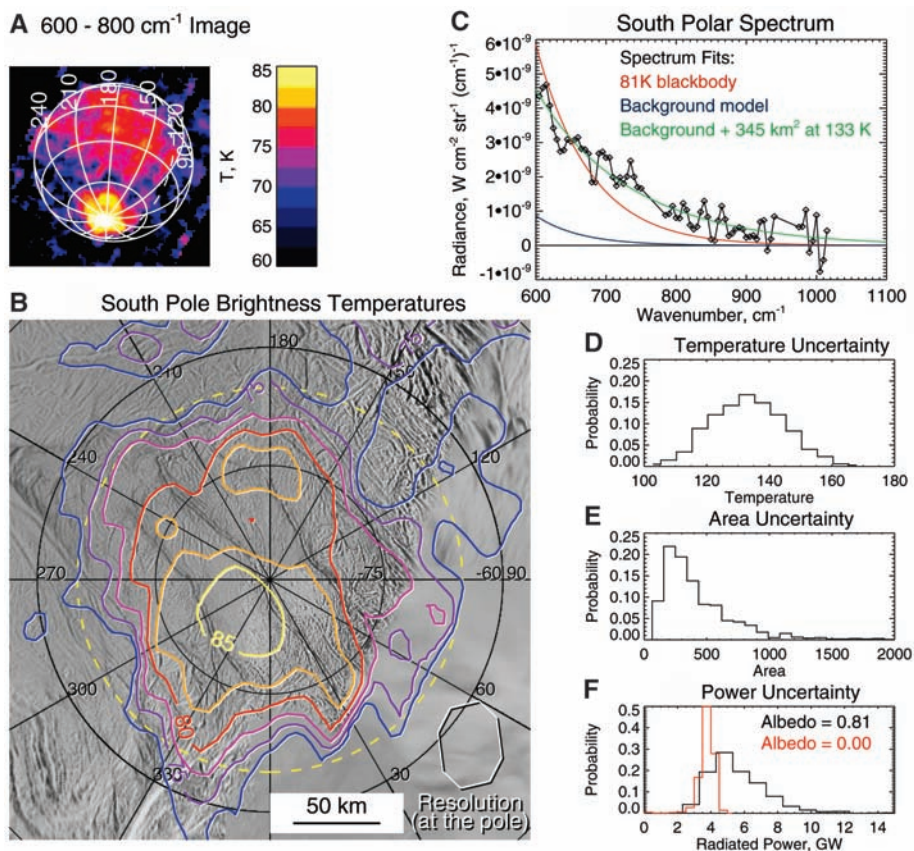

Fig. 2. (**A**) Mid-IR brightness temperature image of Enceladus from orbit 11, showing the prominent south polar hot spot. The dashed line is the terminator. (**B**) Brightness temperature contours derived from the observation in (A), superposed on an ISS base map (*19*), showing the spatial correlation of the hot material with the region containing the tiger stripe troughs. Spatial resolution (lower right) of the temperature map is about 50 km after projection and smoothing. The yellow dashed line shows the latitude boundary of the average spectrum shown in (C). (**C**) Thermal emission spectrum of the region south of latitude 65°S, compared with the best fit blackbody spectrum, which does not match the data, and the best fit graybody plus background model spectrum, which matches the data very well. (**D** to **F**). Probability distributions for the temperature (D), filling factor (E), and total radiated power (F) for the hot material in the south polar region, on the assumption of a single temperature for the hot material, derived by Monte Carlo techniques. The power distribution is shown for assumed hot material albedos of 0.81 and 0.00.

determined noise levels (which are dominated by instrumental noise) from the scatter of the observed spectrum around the best fit model. We then added random noise at that level to the model, refitted the noisy model spectrum, and repeated this process many times to determine the probability distribution of fit parameters (Fig. 2, D and E). The probability distribution of fitted temperatures (Fig. 2D) suggests that maximum temperatures below 110 K are highly unlikely.

The spectral fits allow estimation of the total radiated power from the south polar region. After adjusting fitted temperatures for the thermal contribution expected from sunlight absorbed by the hot regions, and assuming that the hot sources have the same albedo ($\sim$0.81) as the rest of the surface, we derived a radiated nonsolar power of 5.8 ± 1.9 GW (Fig. 2F). Even if the hot sources have an albedo of 0.0 (highly unlikely but not formally ruled out, because the hot regions could be mixed with higher albedo regions on spatial scales too small to be resolved), the nonsolar power is still 3.9 GW. These estimates do not include the potential power contributions from the kinetic and latent heat of the south polar plume seen by other Cassini instruments (21–25), or any heat radiated at lower temperatures. For comparison, the total endogenic power radiated by Io is $\sim$10^5 GW (32), and Enceladus' power generation per unit volume, assuming all the heat escapes from the south pole, is 3% that of Io. Assuming that the heat is generated below the surface, the average heat flow over the region south of 65°S is 0.25 W m^{-2}, compared with $\sim$2.5 W m^{-2} for Io (32). The depth to melting or to ice warm and ductile enough to transport heat by convection, assuming pure solid H$_2$O ice and an ice conductivity of 3×10^5 erg cm^{-1} s^{-1} K^{-1} at the mean temperature of 180 K (33), is then only 2.5 km if the heat is generated below this level. In the hot regions at 124 K, heat flow is 13 W m^{-2}, and solid H$_2$O ice will approach the melting temperature at a depth of only 40 m. It is perhaps more likely that the heat is transported to the surface by advection of warm vapor rather than by conduction.

The relationship to the geological features becomes clearer in higher resolution CIRS observations obtained during the last 2.5 hours of the approach to Enceladus. In this period, CIRS did not perform contiguous scans of Enceladus, but instead rode along with the pointing determined by the ISS cameras as they obtained imaging mosaics of the moon, resulting in very scattered coverage with mid-IR spatial resolution as fine as 50 m near the closest approach (Fig. 3A). These higher resolution observations confirm that the thermal emission is highly localized and is associated with individual prominent tiger stripe troughs (19). The spatial correlation is not perfect, but discrepancies can perhaps be ascribed to pointing uncertainties. In some cases, the pointing uncertainties can be eliminated, because CIRS observations were obtained near-simultaneously with
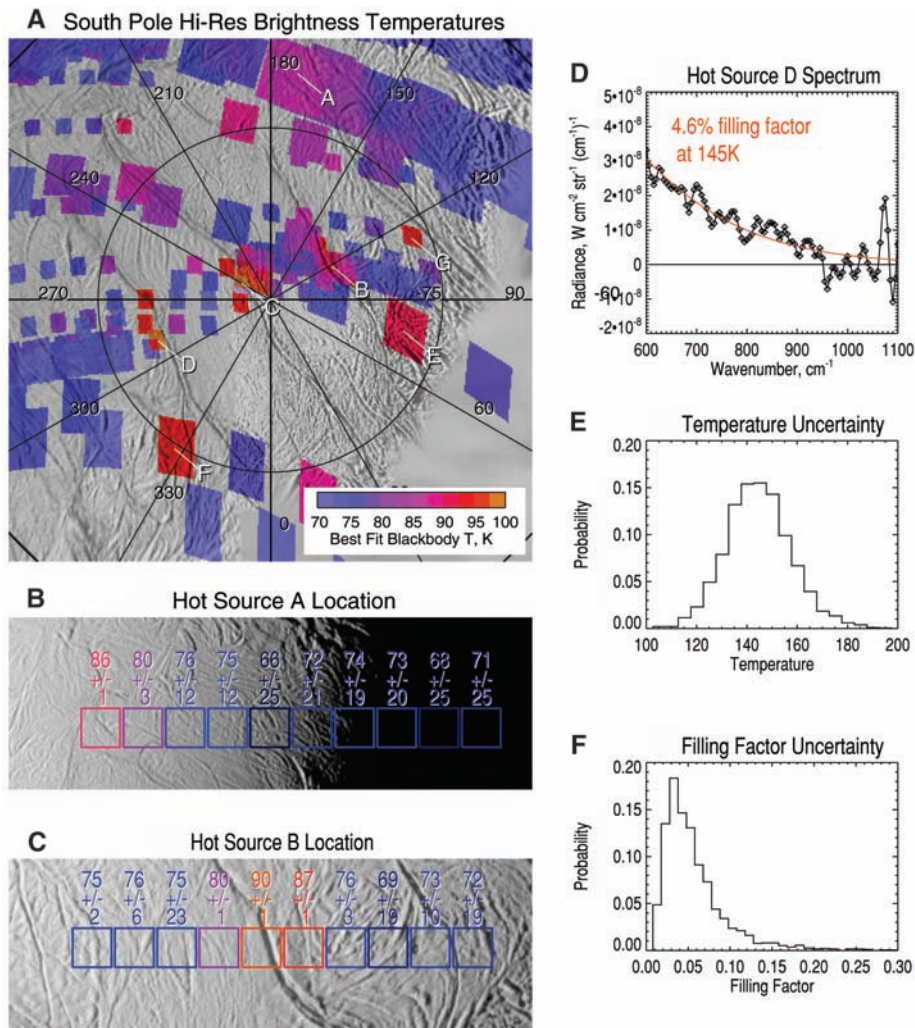

Fig. 3. (**A**) Color-coded south polar brightness temperatures at high spatial resolution, derived from the ISS ride-along CIRS observations, superposed on an ISS base map (19). This shows the correlation between high brightness temperatures and the individual tiger stripe troughs. Isolated colored rectangles represent observations taken during slews, and these have less reliable locations than other observations. The locations of the seven hot sources described in Table 2 and the rest of this figure are indicated. (**B** and **C**) Precise location of hot sources A and B relative to the topography as derived from simultaneous ISS images (19). Each box shows a single mid-IR field of view and its associated brightness temperature, with uncertainties. Field of view size is 17.5 km for source A and 6.0 km for source B. (**D**) The hottest individual CIRS spectrum (source D) and the best fit graybody spectrum. (**E** and **F**) Probability distribution of the temperature and filling factor for the spectrum of source D, assuming a single temperature.

Table 2. Selected discrete hot sources identified by CIRS.

Hot source designation	Latitude	Longitude	CIRS resolution (km)	Best fit graybody		
				Temperature	Filling factor	Width if linear
A	69°S	171°W	17.5	114 ± 22	0.063	1100 m
B	84°S	137°W	6.0	117 ± 16	0.092	550 m
C	87°S*	236°W*	5.8	135 ± 9	0.082	480 m
D	80°S*	289°W*	5.8	145 ± 14	0.046	250 m
E	78°S*	78°W*	13.6	133 ± 28	0.035	480 m
F	75°S*	328°W*	13.3	157 ± 24	0.017	230 m
G	76°S*	115°W*	6.0	127 ± 28	0.053	320 m

*Approximate location, no simultaneous imaging.

camera exposures, and because the ISS field of view includes the 1×10–pixel CIRS mid-IR field of view. The location of the thermal emission observations relative to the geological features can then be determined very precisely (Fig. 3, B and C), confirming the association with the troughs, although there also seems to be some thermal emission from regions adjacent to the troughs. Table 2 describes the seven discrete hot sources that can be identified with greatest confidence in the ride-along observations, either because of simultaneous imaging or particularly strong thermal emission (Fig. 3A). We fitted blackbodies to the spectra of these sources after subtracting spectra of adjacent regions taken with the same CIRS detector, thus removing, to first order, the small contribution of thermal emission from the background and reducing calibration uncertainties. The association of the hot sources with linear features makes it likely that the hot sources are themselves linear, and Table 2 lists the inferred width of each source on the assumption that it is a linear feature extending across and beyond the CIRS field of view. The hot regions appear to be typically hundreds of meters wide. Some of the hottest individual spectra (sources C to G) were obtained during slews between ISS mosaic positions, and thus cannot be located so precisely, although they also appear to be close to the tiger stripe troughs. The brightest spectrum, D, requires a temperature of 145 ± 14 K, with temperatures below 120 K being highly unlikely (Fig. 3, D to F).

CIRS observed the north pole of Enceladus after the closest approach, and although mid-IR coverage is more limited than at the south pole, we can rule out a similar hot spot in the north. A far-IR integration of an 80-km-diameter region centered on the north pole, which has been in darkness since 1995, determined a best fit temperature of 32.9 ± 1.2 K (Fig. 1C). To be conservative, however, this should be considered an upper limit because of the possibility that scattered radiation from surrounding warmer regions contaminated the signal. The corresponding thermal inertia, averaged over the penetration depth of the seasonal thermal wave (about 1 m), is <100 J m^{-2} s$^{-\frac{1}{2}}$ K^{-1}. Any north polar hot component at the temperature of the south polar spot (133 K) would have to have less than 15% of the heat flow of the south polar spot in order to avoid detection in this integration. The lack of a north polar hot spot is consistent with the presence of heavily cratered terrain at the north pole (*4, 6*).

Discussion. It is likely that these warm troughs are the source of the dust and vapor plume seen by other Cassini instruments (*21–25*). From a stellar occultation measurement, UVIS detected a vapor plume above the south polar region (*22*) and determined an escape rate of 5×10^{27} to 10×10^{27} molecules per second. If we assume that the immediate origin of this plume is thermal sublimation of warm water ice (or the plume is in

vapor pressure equilibrium with surface ice at its source) and that this warm ice is visible to the CIRS instrument (rather than being hidden in deep fractures, for instance), we can constrain the temperature of the plume source using the observed thermal emission from the south pole. The mean south polar radiance at 900 cm^{-1}, about 5×10^{-10} W cm^{-2} str^{-1} (cm^{-1})$^{-1}$ (Fig. 2C), places an upper limit on the exposed area of a high-temperature plume source at a given temperature; thus, by using the vapor pressure curve for water ice (*34*), these results also place an upper limit to the sublimation rate from this source. The UVIS escape rate can be reconciled with the observed 900-cm^{-1} radiance only for plume source temperatures of 180 K or higher. A 180 K plume source would have an area of 28 km^2, equivalent, for instance, to a 50-m width along each of the four ~130-km-long tiger stripes (*19*), to produce the UVIS lower limit H$_2$O flux. 180 K is close to the 173 K temperature of a water/ammonia eutectic melt, a plausible cryovolcanic fluid within Enceladus (*14*), but the correspondence may be coincidental, because ammonia was not detected in the plume by the INMS instrument (*23*). The 345-km^2 area of the south polar warm material (Fig. 2B) is consistent with all the warm material being concentrated along the tiger stripes, with a mean width for the warm material of ~660 m, roughly consistent with the widths inferred from the high-resolution samples (Table 2).

The presence of these high temperatures at the south pole of Enceladus is surprising. As described above, the temperatures in many places are too high to be caused by simple re-radiation of sunlight absorbed at the surface. Very high subsurface temperatures can, in theory, be produced by subsurface trapping of solar radiation—the so-called solid-state greenhouse effect (*35*)—and might generate warm gases that could escape along fractures and form plumes, as has been proposed for Neptune's moon Triton (*36*). However, sufficiently large temperature enhancements have not been demonstrated in practice, and the association of the heat with obviously endogenic geological features (*19*) also makes a solar heating origin unlikely. An endogenic heat source is thus the most plausible explanation for the high temperatures. Maximum available power from radiogenic heat, assuming a chondritic composition for the nonice material in Enceladus, is about 0.1 GW (*15*), much smaller than observed. But tidal heating might generate 10 to 100 times more heat (*37*), which is comparable to the observed value. It is also possible that Enceladus is in an oscillatory state, as has been proposed for Io and Europa (*38*). In that case, its eccentricity and tidal heating rate may have recently been much higher, and perhaps the moon is still cooling down from that period.

The Cassini CIRS instrument has found that Enceladus is radiating at least several gigawatts of endogenic heat at temperatures of up to 145 K or

higher. Comparison with ISS images (*39*) shows that most or all of the heat is concentrated along surface troughs. These warm troughs are presumably the source of the vapor and dust plumes seen by other Cassini instruments.

References and Notes
1. D. P. Cruikshank, *Icarus* **41**, 246 (1980).
2. J. P. Emery, D. M. Burr, D. P. Cruikshank, R. H. Brown, J. B. Dalton, *Astron. Astrophys.* **435**, 353 (2005).
3. S. F. Dermott, P. C. Thomas, *Icarus* **109**, 241 (1994).
4. B. A. Smith *et al.*, *Science* **215**, 505 (1982).
5. A. J. Verbiscer, R. G. French, C. A. McGhee, *Icarus* **173**, 66 (2005).
6. J. S. Kargel, S. Pozio, *Icarus* **119**, 385 (1996).
7. B. J. Buratti, *Icarus* **75**, 113 (1988).
8. M. Horanyi, J. A. Burns, D. P. Hamilton, *Icarus* **97**, 248 (1992).
9. K. D. Pang, C. C. Voge, J. W. Rhoads, J. M. Ajello, *J. Geophys. Res.* **89**, 9459 (1984).
10. P. K. Haff, G. L. Siscoe, A. Eviatar, *Icarus* **56**, 426 (1983).
11. W. B. McKinnon, *Lunar Planet. Sci. Conf.* **14**, 487 (1983).
12. D. P. Hamilton, J. A. Burns, *Science* **264**, 550 (1994).
13. S. Jurak, R. E. Johnson, J. D. Richardson, *Icarus* **149**, 384 (2001).
14. S. W. Squyres, R. T. Reynolds, P. M. Cassen, *Icarus* **53**, 319 (1983).
15. G. Schubert, T. Spohn, R. T. Reynolds, in *Satellites*, J. Burns, M. Matthews, Eds. , (Univ. of Arizona Press, Tucson, AZ, 1986), pp. 224–292.
16. M. N. Ross, G. Schubert, *Icarus* **78**, 90 (1989).
17. L. Czechowski, J. Leliwa-Kopystyński, *Planet. Space Sci.* **53**, 749 (2005).
18. J. Wisdom, *Astron. J.* **128**, 484 (2004).
19. C. C. Porco *et al.*, *Science* **311**, 1393 (2006).
20. R. H. Brown *et al.*, *Science* **311**, 1425 (2006).
21. M. K. Dougherty *et al.*, *Science* **311**, 1406 (2006).
22. C. J. Hansen *et al.*, *Science* **311**, 1422 (2006).
23. J. H. Waite Jr. *et al.*, *Science* **311**, 1419 (2006).
24. R. L. Tokar *et al.*, *Science* **311**, 1409 (2006).
25. F. Spahn *et al.*, *Science* **311**, 1416 (2006).
26. M. Flasar *et al.*, *Space Sci. Rev.* **115**, 169 (2004).
27. R. Hanel *et al.*, *Science* **215**, 544 (1982).
28. Brightness temperature is the temperature of a blackbody emitting the observed flux at the observed wavelength.
29. Thermal inertia, defined as $\sqrt{(k\rho c)}$, where k is the thermal conductivity, ρ is the density, and c is the specific heat, describes the ability of a surface to resist temperature changes caused by changes in insolation.
30. B. Buratti, J. Veverka, *Icarus* **58**, 254 (1984).
31. J. R. Spencer *et al.*, in *Pluto and Charon*, S. A. Stern, D. Tholen, Eds. (Univ. of Arizona Press, Tucson, AZ, 1997), pp. 435–473.
32. A. S. McEwen, L. P. Keszthelyi, R. Lopes, P. M. Schenk, J. R. Spencer, in *Jupiter, the Planet, Satellites, and Magnetosphere*, F. Bagenal, T. Dowling, W. McKinnon, Eds. (Cambridge Univ. Press, Cambridge, UK, 2004), pp. 307–328.
33. J. Klinger, *Science* **209**, 271 (1980).
34. C. E. Bryson, V. Cazcarra, L. L. Levenson, *J. Chem. Eng. Dat.* **19**, 107 (1974).
35. D. L. Matson, R. H. Brown, *Icarus* **77**, 61 (1989).
36. R. H. Brown, R. L. Kirk, T. V. Johnson, L. A. Soderblom, *Science* **250**, 431 (1990).
37. L. Czechowski, paper presented at the 35th Committee on Space Research (COSPAR) Scientific Assembly, Paris, France, 18 July 2004.
38. H. Hussmann, T. Spohn, *Icarus* **171**, 391 (2004).
39. CIRS and ISS are acknowledged in the codiscovery of the correlation between the hot spots and the tiger stripe fractures.
40. We acknowledge the invaluable support of the entire Cassini science and engineering teams in making these observations possible. The work was supported by the NASA Cassini Project.